International Conference on Space Optics—ICSO 2004

Toulouse, France

30 March–2 April 2004

Edited by Josiane Costeraste and Errico Armandillo

Laboratory test of an APS-based sun sensor prototype

Giancarlo Rufino, Alessandro Perrotta, Michele Grassi

International Conference on Space Optics — ICSO 2004, edited by Errico Armandillo, Josiane Costeraste, Proc. of SPIE Vol. 10568, 105680Z · © 2004 ESA and CNES
CCC code: 0277-786X/17/$18 · doi: 10.1117/12.2307972

LABORATORY TEST OF AN APS-BASED SUN SENSOR PROTOTYPE

Giancarlo Rufino[(1)], Alessandro Perrotta[(2)], and Michele Grassi[(3)]

DISIS – Dipartimento di Scienza e Ingegneria dello Spazio – Università di Napoli Federico II
Piazzale Tecchio 80 - 80125 Napoli – Italy
[(1)]giancarlo.rufino@unina.it, [(2)]perrotta_alessandro@yahoo.it, [(3)]michele.grassi@unina.it

ABSTRACT

This paper deals with design and prototype development of an Active Pixel Sensor – based miniature sun sensor and a laboratory facility for its indoor test and calibration. The miniature sun sensor is described and the laboratory test facility is presented in detail. The major focus of the paper is on tests and calibration of the sensor. Two different calibration functions have been adopted. They are based, respectively, on a geometrical model, which has required least-squares optimisation of system physical parameters estimates, and on neural networks. Calibration results are presented for the above solutions, showing that accuracy in the order of 0.01° has been achieved. Neural calibration functions have attained better performance thanks to their intrinsic auto-adaptive structure.

1. INTRODUCTION

Over the last few years micro- and nano-satellites have received great attention due to several factors: reduced costs and frequent opportunity for launch, chance for cost-effective flight validation of innovate technologies for major applications, increased on-board functionality thanks to technology progress, new concepts of distributed spacecraft/payload [1,2]. This is still the current trend, while more and more challenging mission objectives are being conceived for these spacecraft because of the continuous technology progress that makes stringent requirements on platform performance feasible in spite of on-board modest power and mass resources. A major role is played by Micro – Electro – Mechanical - System (M E M S) technology, which is evolving quickly [3]. In fact, such a spacecraft is bound to low-power, compact, light on-board devices, but, at the same time, high performance is required to the bus since mission objective are not restricted. Miniature digital star sensor are valid candidates for this modern applications since they benefit of the most recent technology advances in electronics and photodetectors [4,5,6] and they show interesting features in terms of performance, reliability, and on-board resource utilization.
In this framework, starting from the expertise gained in the development of a CCD-based star sensor prototype [7], the aerospace plans and systems team at the university of Naples has developed an Active Pixel Sensor (APS) – based miniature sun sensor and a laboratory facility for its indoor test and calibration. These activities are part of a joint project of the University of Naples Federico II with other Italian universities, under the financial sponsorship of the Italian Space Agency and the Italian Ministry of University and Scientific Research, for design and prototype development of four, 10-kg nanosatellites to be flown in formation for remote sensing applications and for demonstration of technological issues related to formation flying, such as autonomous guidance, navigation, and control. This paper presents the developed sensor prototype and, in more detail, the laboratory facility. Also, the calibration campaign for the developed sensor is described and results are reported.

2. THE LABORATORY TEST FACILITY

The laboratory facility has been conceived to test the basic functionality of a wide-FOV sun sensor, that is measuring the direction along which the sensor is illuminated by a radiating source, the sun, located at a distance of approximately 1 AU with an apparent angular size of 0.53°. To the aim of thorough and effective test capability, variable illumination direction has been envisaged as well as high-accuracy in its control. Attention has been paid to sun radiating flux characteristics, i.e., spectral composition and density, since they influence the sensor detector response and, hence, the sensor output. In fact, it is necessary that real operative condition are reproduced as far as possible during test and calibration for they validity.
The realised system consists of four main sections: radiation source, collimating optics, sensor micro-positioning subsystem, PC-based control terminal. They have been set up to reproduce a light source that appears to the sensor under test as the sun appears in the operative conditions described above and allow for sensor - light source relative pointing control. These components have been installed on an optical table for stable and precise alignment. A dark room set-up covers all the components to isolate them from external light sources and avoid internal reflections (Fig. 1).

2.1 Radiation Source Subsystem

A 1000-W Xenon arc-lamp by Oriel Instruments™ has been selected as radiation source. In fact, the spectrum of emission of this kind of lamp allows them to be used in sun simulators when the spectral region from 200 nm to 2500 nm is of interest [8]. The latter is wider than the one necessary for the present application, that is determined by the detector spectral response (400-1000 nm). The lamp is powered by a stabilised 70-Vdc supplier with controllable output power in the range 450-1000W. The housing where the lamp is installed is equipped with a water filter to cut infrared emission beyond 1200 nm, and optics that focus the light in a 48 mm-diameter collimated beam [8]. This output is conveyed by a special adapter and a fiber optic to a 10 cm-diameter integrating sphere by Labsphere™. Its internal surface with Spectraflect™ coating guarantees diffuse reflection and low loss (reflection coefficient equal to 0.977 @ 600 nm [9]). At its output port a diffuse and highly uniform emission is available, as desired. It supplies a light source adequate to illuminate the sensor under test.

2.2 Collimating Optics

In real operating condition, the radiation illuminating the sensor is practically collimated as a result of the large distance from the sun. Of course, the angular spread of light rays consequent to the finite angular size of the sun is present. This is reproduced by installing a collimating optics before the sensor at a distance from the sphere output port equal to its focal length. The latter has been chosen equal to 1.5 m to satisfy size constraints of the facility. Consequently, a 13.7 mm-diameter circular aperture has been installed at the output port to obtain the desired angular size (0.53°) of the uniform source. In this configuration, the radiant flux density of the sun has not been reproduced because it would require very high power levels and hardware complexity. On the other hand, satisfactory test can be carried out after increasing the sensor shutter time so that the selected average pixel output at the spot centre is obtained. This value has been set to 80% of the linear response limit of the pixel. Of course, this approach leads to conservative results in terms of sensor measurement accuracy because increased noise levels are present in this case due to dark current effects for longer exposure time.

2.3 Sensor Micropositioning Subsystem

The function of this section of the facility is to accommodate the sensor in the test camera and to orientate it with respect to the light source. It has been designed to allow one to control sensor boresight and to modify it by means of rotations along two axes (axis 1 is vertical, axis 2 is horizontal) that are perpendicular to each other and both to the longitudinal axis of the system, coincident with both the collimator optical axis and the integrating sphere output port axis. Relative motion has been realised by means of three high-precision micro-translators and two rotation stages by Physik Instrumente™. The subsystem is based on a three-dimensional micro-translator which has been introduced to operate the fine alignment of sensor boresight to source boresight and collimator optical axis. It has been realised by stacking a vertical translator and two horizontal ones. They can be adjusted manually and guarantee 2.5μm of accuracy [10]. The two rotation stages, whose main features are in tab. 1, are moved by servomotors and controlled via a PC serial link. The first rotation stage is installed on

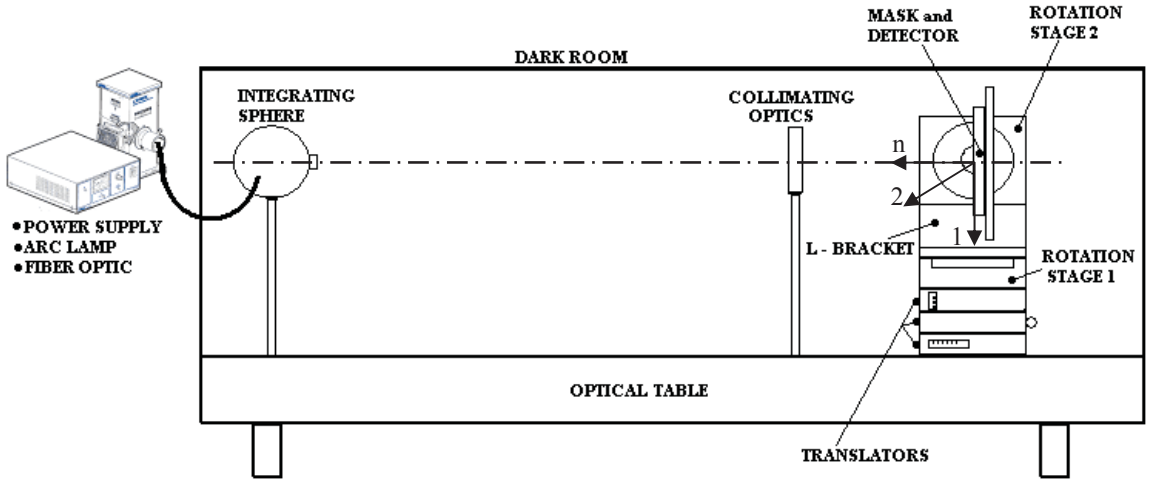

Fig. 1. Laboratory test facility configuration.

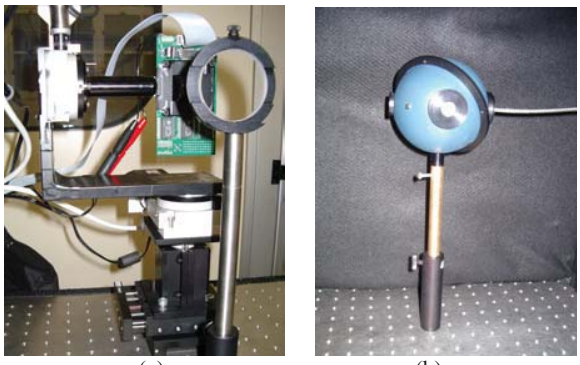

(a) (b)

Fig. 2. Micropositioning subsystem and collimator (a), and integrating sphere (b).

the top of the three-dimensional translator. It operates rotations along axis 1. An L-shaped aluminium bracket has been specifically designed to assemble the second rotation stage in order that it operates axis 2 rotations. The bracket has been designed in conjunction with the holder that fixes the sensor under test to the micropositioning subsystem so that in the nominal configuration the two rotation axes and the sensor boresight are mutually perpendicular and they intersect at the mask centre. As a result, axis 1, axis 2, and sensor boresight axis (n) can be assumed as the sensor-fixed reference frame when the sensor is installed in the test camera. Bracket and holder have been realised with reference to the sensor hardware prototype described in the following. Their design included accurate analysis of static deformations, kept within the rotation stage wobble (150 μrad). Analogously, machining tolerances have been assigned to guarantee that orientation uncertainty of the sensor after installation is within the same value. Finally, bracket size was constrained to avoid interference with sensor FOV up to ±60° off-boresight.

Rotation range	Continuous
Design resolution	0.001°
Min. incremental motion	0.001°
Max. velocity	90°/s
Unidirectional repeatability	0.00342°
Wobble	0.00860°
Encoder resolution	4000 counts/rev
Motor power / voltage range	30 W / 0-24 Vdc
Weight	0.62 kg

Tab. 1. Motorised rotation stage main features [10].

2.4 Control Terminal

The National Instrument LabView™ graphic environment has been selected to develop the control terminal. It has been conceived to command:

- sensor pointing by operating the rotation stages;
- sensor operation (acquisition, shutter time control, acquired image windowing and download).

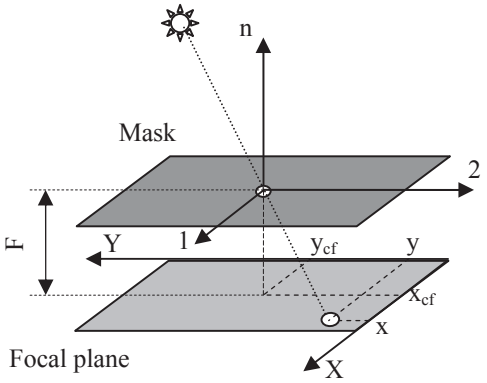

Fig. 3. Sun-line measurement concept.

The serial and the parallel communication ports are used for the first and the second task, respectively. Both channels are bi-directional. In fact, the communication channel to the rotation stages controllers allows one to send commands and also to get information about the status of the stage. This has been exploited when commanding rotations to receive back the measured real position of the platform at accuracy (<1 arcsec) better than command execution (never worse than 9 arcsec during all the performed tests). The measured position has been assumed as reference datum during calibration and measurement accuracy tests. Parallel communication procedure with the detector board has been implemented to upload commands and download acquired images. In addition, the developed control panel has tools to manage automatically campaigns of multiple acquisitions. The user plans the campaign by setting range and step of the two rotation angles, number of acquisitions per pointing, and shutter time. In addition, to reduce the amount of data to be saved, it has been envisaged an option to localise the detector region where the spot has been imaged, cut a windows around it, and download the window (along with its corners' coordinates) instead of full image, thus saving up to 95% of disk space and speeding up the procedure in the same ratio.

3. SUN SENSOR MODEL

The prototype of the miniature sun sensor under development [11] has been tested in the presented laboratory facility. The sensor is based on a radiation-hardened Active Pixel Sensor (APS) detector (STAR250™ by FillFactory), which has an array of 512 x 512 25-μm sensing pixels, and a slim opaque mask with a tiny hole (0.1-μm radius) covering the detector and limiting its illumination. As the sun light passes through the hole, a nearly circular spot is formed on the sensing surface of the detector [Fig. 3]. Due to the distance F between the focal plane and the

mask, representing the focal length of the system, the spot position changes as the illumination direction varies, thus allowing its measurement on the basis of spot centre position. The latter one is computer by centroiding the spot image [12]. Two different configurations have been conceived for the mask. The first one envisages a single hole located over the detector centre. The choice of the focal length F=3 mm determines a symmetrical, square FOV larger than 120°x 120°. In the second configuration, the mask has a 10x10 array of holes and also in this case it is centred over the detector. The FOV size, slightly reduced, is still in the order of 120°x 120°. Such a mask determines an array of spots on the focal plane, so that multiple sun-line measures can be produced, at the cost of increased image processing, and an improved estimate can be produced by averaging. The attainable performance has been preliminarily estimated by means of software simulations of sensor operation [11], which accounted for real sun illumination characteristics and noise characteristics peculiar of the STAR250™ detector. The resulting theoretical accuracy is in the order of 0.005°.

In order to validate design and theoretical performance analysis, a prototype has been realised to carry out tests on real hardware (fig. 4). At a preliminary stage when the major interest is in validating the sensor concept, it has been chosen to develop the hardware model using a low-cost technology and commercial-off-the-shelf electronics to limit costs and shorten procurement time. With regard to the detector, the FillFactory IBIS4™ and its demo-board for control and I/O electronics have been selected. This detector characteristics, in terms of pixel size and noise, allow for output features, in specific operation mode such as pixel binning, that are nearly equivalent to the STAR250 ones. In addition, the demo-board allows for straightforward and efficient detector control, without need for any additional electronics. The mask has been realized by using a 0.1 mm-thick steel foil, on which the holes have been machined by electron discharge. The latter one is a low-cost technique that allows for 0.01-mm accuracy in hole diameter manufacturing. An aluminium element, the holder, has been designed to assembly the mask and the detector installed on its demo-board. This element connects the sensor to the rotation stages in the test camera. These solutions have effects in terms of performance and functionality of the prototype, which results reduced with respect to nominal design. In particular, the adoption of such a “thick” mask determines considerable spot deformations for off-nadir illumination angles larger than 20°-22° and, hence, tests for such cases are not representative of the real, nominal design sensor. Also, adoption of the demo-board electronics strongly slows down image download to the processing unit and makes real time operation tests not feasible. Nevertheless, validation of the sensor concept, of software simulators, of algorithms and procedures is certainly possible and efficient.

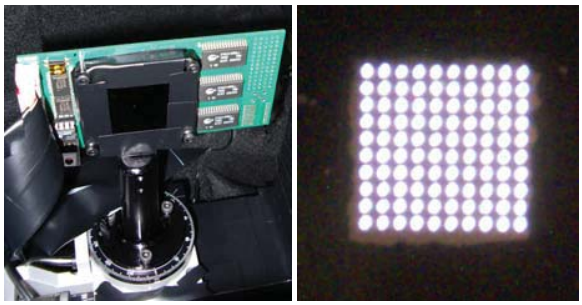

(a) (b)

Fig. 4. Sensor prototype (a) and detail of the multi-hole mask (b).

4. CALIBRATION SOLUTIONS

Fig. 3 shows the concept exploited to measure the sun-line unit vector. With reference to the symbols in figure, the basic model assumes that the sun-line unit vector can be computed in the sensor reference frame (12n) as a function of spot centroid coordinates (x, y) in the focal plane two-dimensional reference frame:

$$\begin{aligned} x &= -F \tan\beta + x_{cf} \\ y &= -F \frac{\tan\alpha}{\cos\beta} + y_{cf} \end{aligned} \qquad (1)$$

where x_{cf} and y_{cf} are the coordinates of the projection of mask centre onto the focal plane, and α and β are the rotation along axis 1 and axis 2, respectively, that, in this sequence, align the sensor boresight axis n to the illumination direction.

This purely geometrical model is not adequate to attain high accuracy in estimating sun-line orientation because spot centroid is not coincident with sun-line intersection on the focal plane for several reason: systematic and random errors affecting centroiding [13], spot asymmetrical deformation for increasing off-boresight illumination, imperfect alignment of system components and machining defects (hence some parameters of the real system, e.g. F, are not equal to design values), etc.. As a consequence, calibration functions of the sensor must be introduced to compensate for errors in the direct geometrical model. Two different approaches have been tried to this aim: the refinement of the geometrical model (1) and the use of Neural Networks (NNs) to map the computed centroid coordinates into sun-line orientations.

4.1 LSQ Geometrical Model

The refinement of the geometrical model has been

based on the hypothesis that the main error source in (1) is due to imperfect values of nominal parameters relevant to the geometrical configuration of the system. In particular, it has been assumed that the real and the nominal configurations are different because:

– the distance between mask and focal plane is not F (nominal value), but F+ΔF;
– the mask plane and the focal plane are not parallel, so that there are offsets (α_0 and β_0) in the angles α and β for boresight illumination along axis n.

In this case, the reference geometrical model is

$$\begin{aligned} x &= -(F+\Delta F)\tan(\beta+\beta_0)+x_{cf} \\ y &= -(F+\Delta F)\frac{\tan(\alpha+\alpha_0)}{\cos(\beta+\beta_0)}+y_{cf} \end{aligned} \qquad (2)$$

In practice, since the uncertainty in x_{cf} and y_{cf} is not negligible because hole location, size, and shape suffer from machining tolerances and assembling accuracy, these equations have not been exploited directly. It has been preferred to express introduce the coordinates x_{zp} and y_{zp} of the spot centre for zenith illumination (α=0, β=0) (fig. 5) that are measured in a specific preliminary test:

$$\begin{aligned} \alpha_m = -\alpha_0 + \tan^{-1}\Bigg[& \frac{1}{F+\Delta F} \\ & \times \cos\left(\tan^{-1}\frac{x_{zp}-x+(F+\Delta F)\tan\beta_0}{F+\Delta F}\right) \\ & \times \left(y_{zp}-y\frac{(F+\Delta F)\tan\alpha_0}{\cos\beta_0}\right)\Bigg] \end{aligned} \qquad (3)$$

$$\beta_m = -\beta_0 + \tan^{-1}\frac{x_{zp}-x+(F+\Delta F)\tan\beta_0}{F+\Delta F}$$

where the symbol α_m and β_m represent the measured rotations along axes 1 and 2, whilst α and β represent the assigned ones.

To estimate ΔF, α_0, and β_0, a least square procedure has been implemented to get the best fit of the assigned rotations along axes 1 and 2 with the relevant measures operated in the test camera for a large number of illumination directions. Due to the non-linearity of the model, the iterative algorithm proposed by Ben-Israel [14,15] was applied, which is based on the local linearization of the problem around the current estimate of the solution. The solution is ΔF=0.094 mm, α_0=1.864°, and β_0=0.415°. They are in accordance with position and shape uncertainty due to machining tolerances of the test system components and of the sensor prototype. The next section reports the description of the data set that was used to carry out the LSQ optimisation and the accuracy achieved by the sensor after exploiting the LSQ-optimised parameters.

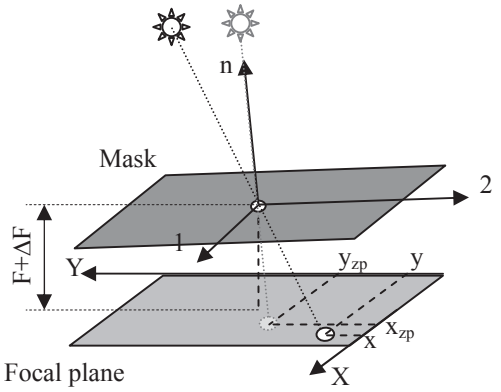

Fig. 5. Refinement of the geometrical model of the system accounting for hardware real configuration.

4.2 Neural Network-based calibration

Three different strategies have been experimented, all based on NNs, to get improved estimates of the illumination direction. In all the cases, two distinct networks have been used for angle α and angle β. The three cases are characterised by different input data, as presented in tab. 2. The same structure has been adopted in all the three cases: feedforward NN with one hidden layer and one output neuron, sigmoid hyperbolic tangent transfer function for the hidden layer, and linear transfer function for the output neuron. This is a quite classic approach when using NNs to approximate complex functions [16,17]. Different numbers (between 20 and 30) of neurons in the hidden layer have been adopted in the three cases and for the two angles on the basis of training results.

	Input	Output
Case 1	Spot centroid coordinates	α angle β angle
Case 2	α and β as computed by model (1) and nominal sensor parameters	α angle β angle
Case 3	α and β as computed by model (3) and LSQ estimate of sensor parameters	α angle β angle

Tab. 2. Input and output of the adopted NNs for sun sensor prototype calibration.

5. TESTS AND RESULTS

A calibration campaign of the sensor prototype equipped with the single-hole mask has been carried out to validate the sensor and the laboratory facility, and to compare the different calibration strategies that have been conceived. Standing first of all these objectives rather than full calibration of the sensor for

operational purpose, attention has been focussed on a reduced subset of the FOV. It has been limited to $-16.5° \le \alpha \le 1.0°$ and $-1.0° \le \beta \le 16.5°$. Three subsets of pointings have been defined (tab. 3) to sample this region of the FOV:

- Training Set (TrS), which has been used for the construction of the calibration functions (both model (3) and NNs);
- Training Test Set (TTS), accurately sampling a region close to the boresight axis, which has been used to check the learning rate during NN training and to appraise close-to-boresight sun-line estimate accuracy;
- Test Set (TS), used to evaluate calibration functions attained performance.

	α angle (°)			β angle (°)		
	from	to	step	from	to	step
TrS	-16.5	0.5	1.0	-0.5	16.5	1.0
$18^2+18+18=$	0	-	-	-0.5	16.5	1.0
360 total samples	-16.5	0.5	1.0	0	-	-
TTS $25^2=$ 625 total samples	-5.0	1.0	0.25	1.0	5.0	0.25
TS	-16.1	0.4	1.5	-0.4	16.1	1.5
$12^2+12+12=$	0	-	-	-0.4	16.1	1.5
168 total samples	-16.1	0.4	1.5	0	-	-

Tab. 3. FOV subsets for construction and validation of the calibration functions.

In the tests, for each illumination direction (fixed α and β) 30 spot images have been acquired and centroided, and the corresponding α_m and β_m have been computed. Then, in order to obtain a noise (random error)-free measure to be used as reference datum in calibration, affected only by the systematic error component, they have been averaged. In fact, only the latter component can be compensated for by calibration. The number of 30 samples has been chosen after analysing the statistics of the preliminary observations for boresight illumination and those of an additional set relevant to the largest separation from the boresight in the considered region. Indeed, assuming Gaussian distribution of the error, the sample variance has been related to the number of samples to be summed so that the computed average of the centroid coordinates differs from the theoretical Gaussian distribution mean less than 1/20 of pixel with 98% confidence. On the other hand, the statistics of measurement errors (deviation of measured angle with respect to assigned one) at each sample of the FOV have been computed to appraise local performance of the sensor. They are referred to as "local" in the following. Furthermore, to get a global figure of merit of the calibrated sensor performance, sample mean and standard deviation have been computed for local average and maximum errors over TrS, TTS, and TS. The symbols μ, σ, M, and σ_M are adopted, respectively, to refer to them. In general, with regard to a specific measurement model including - if present - the calibration function, μ can be regarded as the sensor accuracy, σ relates to its precision in repeated measurements, while M and σ_M may be regarded as worst-case figures of merit.

Preliminarily, the simple geometrical model (1) with nominal parameters (F=3 mm, $\alpha_0=0$, and $\beta_0=0$) has been considered. The relevant global statistics are in tab. 4. The average overall accuracy is as large as 0.20° (TrS ans TS), being in the order of 0.05°-0.08° for TTS that is closer to the boresight. Measurement noise is in the order of 70% of the accuracy, while worst case results are slightly larger (<+10%) than μ.

Model (3) is the basic improvement considered. LSQ optimisation of its parameters has been carried out with reference to TrS samples. Then, illumination direction has been computed for TTS and TS. The relevant local statistics of the measurement errors are in tab. 5. Accuracy of the order of 0.022° and precision of 0.015° are achieved in the average over the whole considered FOV. Typical worst case errors range between 0.028° and 0.050°. The overall enhancement is about one order of magnitude.

		TrS	TTS	TS
$\alpha_m(°)$	μ	0.1716	0.0524	0.1691
	σ	0.1118	0.0334	0.1142
	M	0.1926	0.0749	0.1918
	σ_M	0.1116	0.0343	0.1151
$\beta_m(°)$	μ	0.2587	0.0820	0.2438
	σ	0.1619	0.0511	0.1617
	M	0.2650	0.0871	0.2505
	σ_M	0.1632	0.0513	0.1634

Tab. 4. Global performance of the basic geometrical model (1) (system nominal parameters).

		TrS	TTS	TS
$\alpha_m(°)$	μ	0.0230	0.0299	0.0237
	σ	0.0164	0.0130	0.0136
	M	0.0416	0.0497	0.0438
	σ_M	0.0181	0.0126	0.0174
$\beta_m(°)$	μ	0.0202	0.0096	0.0211
	σ	0.0141	0.0064	0.0177
	M	0.0263	0.0143	0.0277
	σ_M	0.0148	0.0066	0.0194

Tab. 5. Global performance of model (3) calibration function with LSQ-optimised parameters.

All the NN-based calibration functions have been trained using TrS samples following the train-by-epoch backpropagation algorithm [16]. Procedures of the MATLAB™ Neural Network toolbox have been used. TTS samples have been exploited for additional checks aimed at avoiding network overfitting, i.e., extreme specialisation of the neural function for training samples at the expense of reduced ability in generalising the mapping to other cases. TTS samples, which do not influence NN weight adjustment in

training, allow for identification of learning trends leading to loss of generalisation ability (fig. 6). Finally, the achieved performance has been apprised by examining network errors in the TS samples. Tab. 6, tab. 7, and tab. 8 show the global statistics for the three considered cases. The performance of NN 1 and NN 2 are practically coincident, while NN 3 performance is slightly worse. A definite improvement is brought in by NNs with respect to model (3). In fact, accuracy and precision improve, respectively, to 0.020° and 0.011° for α_m, and even to 0.010° and 0.007° for β_m. Typical worst cases result limited to the ranges 0.040°±0.015°(1σ) for α_m and 0.017°±0.009°(1σ) for β_m.

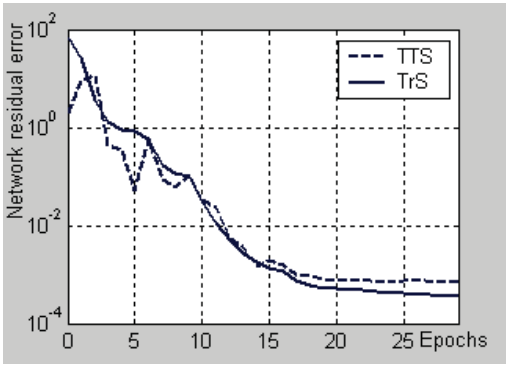

Fig. 6. Typical learning curves during NN training for TTS and TrS (Case3, NN for angle α).

		TrS	TTS	TS
α_m(°)	μ	0.0150	0.0200	0.0189
	σ	0.0086	0.0119	0.0107
	M	0.0333	0.0397	0.0390
	σ_M	0.0123	0.0147	0.0163
β_m(°)	μ	0.0074	0.0073	0.0105
	σ	0.0049	0.0047	0.0074
	M	0.0133	0.0121	0.0171
	σ_M	0.0063	0.0054	0.0095

Tab. 6. Global performance of NN 1 calibration function.

		TrS	TTS	TS
α_m(°)	μ	0.0165	0.0201	0.0182
	σ	0.0100	0.0111	0.0101
	M	0.0350	0.0402	0.0385
	σ_M	0.0143	0.0150	0.0151
β_m(°)	μ	0.0062	0.0079	0.0107
	σ	0.0043	0.0050	0.0076
	M	0.0120	0.0128	0.0174
	σ_M	0.0057	0.0060	0.0097

Tab. 7. Global performance of NN 2 calibration function.

		TrS	TTS	TS
α_m(°)	μ	0.0186	0.0232	0.0213
	σ	0.0113	0.0137	0.0137
	M	0.0372	0.0434	0.0420
	σ_M	0.0151	0.0164	0.0187
β_m(°)	μ	0.0072	0.0087	0.0134
	σ	0.0048	0.0057	0.0120
	M	0.0131	0.0135	0.0201
	σ_M	0.0061	0.0066	0.0142

Tab. 8. Global performance of NN 3 calibration function.

To show the spatial dependency of residual errors after calibration, statistics of the local features have been computed within sub-regions of the considered FOV. They are reported in tab. 9 for model (3) and in tab. 10 for NN 1 that can be assumed as representative of the NN approach because of the analogous behaviour of the three neural calibration functions. These results do not point out a systematic error dependence on illumination boresight, which could be expected, but a rather irregular behaviour. However, σ has the same order of magnitude in the two cases for both angles, so it adequately represents the noise affecting equally the measurements. Also, in most cases the error in β_m is much lower than the one in α_m. The reason for this needs to be investigated. It could be related to a specific behaviour of one of the rotation stages or to the major complexity of the analytical model relating α_m to centroid coordinates. Furthermore, a contribution to non-uniform behaviour of β_m results certainly from APS column noise and it is to be identified by *ad hoc* tests.

β (°)		α (°) -16.1		-11.6		-5.6		0.4	
-0.4		α_m(°)	β_m(°)	α_m(°)	β_m(°)	α_m(°)	β_m(°)	α_m(°)	β_m(°)
	μ	0.0232	0.0129	0.0240	0.0149	0.0332	0.0138		
	σ	0.0135	0.0104	0.0145	0.0087	0.0186	0.0085		
	M	0.0455	0.0182	0.0408	0.0193	0.0540	0.0181		
5.6	σ_M	0.0237	0.0104	0.0106	0.0081	0.0234	0.0085		
	μ	0.0202	0.0159	0.0173	0.0193	0.0284	0.0276		
	σ	0.0125	0.0080	0.0103	0.0109	0.0140	0.0110		
	M	0.0431	0.0232	0.0338	0.0253	0.0484	0.0330		
11.6	σ_M	0.0219	0.0084	0.0101	0.0103	0.0124	0.0100		
	μ	0.0207	0.0435	0.0160	0.0261	0.0235	0.0220		
	σ	0.0106	0.0390	0.0064	0.0155	0.0109	0.0119		
	M	0.0438	0.0535	0.0393	0.0354	0.0401	0.0319		
16.1	σ_M	0.0126	0.0432	0.0140	0.0172	0.0137	0.0127		

Tab. 9. FOV sub-region statistics for model (3) measurement error.

β (°)	α (°)	-16.1		-11.6		-5.6		0.4	
-0.4		α_m(°)	β_m(°)	α_m(°)	β_m(°)	α_m(°)	β_m(°)	α_m(°)	β_m(°)
	μ	0.0204	0.0098	0.0250	0.0076	0.0245	0.0093		
	σ	0.0097	0.0057	0.0171	0.0037	0.0119	0.0061		
	M	0.0446	0.0156	0.0423	0.0116	0.0453	0.0136		
5.6	σ_M	0.0197	0.0071	0.0181	0.0041	0.0197	0.0062		
	μ	0.0128	0.0131	0.0137	0.072	0.0138	0.0088		
	σ	0.0062	0.0067	0.0053	0.0037	0.0072	0.0062		
	M	0.0353	0.0198	0.0302	0.0127	0.0321	0.0149		
11.6	σ_M	0.0166	0.0078	0.0096	0.0042	0.0135	0.0071		
	μ	0.0181	0.0209	0.0187	0.0109	0.0189	0.0095		
	σ	0.0079	0.0109	0.0095	0.0074	0.0077	0.0068		
	M	0.0412	0.0310	0.0406	0.0194	0.0363	0.0191		
16.1	σ_M	0.0094	0.0142	0.0178	0.0093	0.0100	0.0094		

Tab. 10. FOV sub-region statistics for NN 1 measurement error.

6. CONCLUSIONS AND FURTHER WORK

A laboratory facility for sun sensor indoor testing has been designed and developed to validate the hardware prototype of a miniature sun sensor under study at the university of Naples. In particular, the basic configuration of the sensor has been tested. Calibration has been carried out considering two different approaches: a geometrical model with LSQ optimisation of the estimates of system relevant parameters and neural calibration functions. The results of the performed calibration campaign have pointed out that the first model allows for sun-line measurement accuracy in the order of 0.020°, while the neural network-based solution offers improved performance up to 0.01°. Nevertheless, further studies are necessary for in-depth characterisation of the sensor response, to identify the sources of the experienced residual errors in order to achieve better compensation for them, and to refine the adopted model. In addition, a new calibration campaign has to be carried out to validate the improved configuration of the sensor. Based on the multi-hole mask, the last one allows for multiple measurements of the sun-line orientation in a single acquisition so that sensor accuracy will improve as a result of averaging multiple simultaneous measurements.

7. REFERENCES

1. I. Bekey, *Advanced Space System Concepts and Technology: 2010-2034+*, AIAA, El Segundo (CA), USA, 2003.

2. D. Collins, K Kukkonen, and S. Veneri , Miniature, "Low Cost, Highly Autonomous Spacecraft-A Focus on New Millennium," IAF Paper 95-U.2.06, 46th International Astronautical Congress, Oslo, Norway, 1995.

3. *Proceedings of the 2nd Round Table on Micro/Nanotechnology for Space*, ESTEC, the Netherlands, 15-17 Oct 1997, ESA WPP-132.

4. E. R. Fossum, CMOS Image Sensors: Electronic Camera-On-A-Chip, *IEEE Trans. on Electron. Devices*, Vol. 44, No. 10, pp. 1689-1698, 1997.

5. J. H. Hales and M. Pedersen, "Two-axis MOEMS Sun Sensor for Pico Satellites," 16th Annual AIAAA/USU Conf. on Small Satellites, 2001.

6. C. C. Liebe, S. Mobasser, C. J. Wrigley, Y. Bae, A. Howard, J. Schroeder, "Micro Sun Sensor," *Proc. 2002 IEEE Aerospace Conf.*, paper #274. Big Sky (MT), USA, 2002.

7. G. Rufino and D. Accardo, "An Effective Procedure to Test Star Tracker Software Routines Using a Sensor Model," *Proc. 4th Int.Conf. on Space Optics*, 5-7 Dec 2000, Tolouse, France, pp.703-712.

8. Catalog *Solar Simulation*, Oriel Corporation, Stratford (CT), USA, 1993.

9. 2000-2001 Catalog *Sphere Systems and Instrumentation*, Labsphere, North Sutton (NH), USA.

10. Catalog *MicroPositioning, NanoPositioning, NanoAutomation*, Physik Instrumente (PI) GmbH, Karsruhe, Germany, 2001.

11. M. Buonocore, M. Grassi, and G. Rufino, "APS-based Miniature Sun Sensor for Earth Observation Nanosatellites", *4th IAA Symp. on Small Satellites for Earth Observation*, Berlino (D), 7-11 Apr 2003, paper IAA-B4-0703, 7pp.

12. W. K. Pratt, *Digital Image Processing*, 2nd edition, John Wiley and Sons, New York, USA, 1991.

13. G. Rufino and D. Accardo, "Enhancement of the Centroiding Algorithm for Star Tracker Measure Refinement," *Acta Astron.*, Vol. 53, No. 2, 2003, pp. 135-147.

14. A. Ben-Israel and T. N. E. Greville, *Generalized Inverse: Theory and Applications*, John Wiley and Sons, New York, USA, 1974.

15. D. P. Bertsekas, *Nonlinear Programming*, Athena Scientific, Belmont (MA), 1995.

16. H. Demuth and M. Beale, *Neural Network Toolbox For Use with MATLAB*, vers. 4, The MathWorks, Natick (MA), USA, 2001.

17. M. T. Hagan and M. B. Menhaj, "Training feedforward networks with the Marquardt algorithm," *IEEE Trans. on Neural Networks*, Vol. 5, No. 6, 1994, pp. 989 – 993